International Journal of Thermofluids 27 (2025) 101185

Contents lists available at ScienceDirect

International Journal of Thermofluids

journal homepage: www.sciencedirect.com/journal/international-journal-of-thermofluids

On the effect of fluid temperature in hydrodynamic cavitation on a chip reactors

Seyedreza Tebyani [a,b], Farzad Rokhsar Talabazar [a,b], Morteza Ghorbani [a,b,c,d,*], Ali Koşar [a,b,c,*]

[a] Faculty of Engineering and Natural Sciences, Sabanci University, 34956 Tuzla, Istanbul, Turkey
[b] Sabanci University Nanotechnology Research and Application Center, 34956 Tuzla, Istanbul, Turkey
[c] Center of Excellence for Functional Surfaces and Interfaces for Nano-Diagnostics (EFSUN), Sabanci University, Orhanli, 34956, Tuzla, Istanbul, Turkey
[d] School of Engineering, Computing and Mathematics, Oxford Brookes University, College Cl, Wheatley, Oxford, OX33 1HX, UK

ARTICLE INFO

Keywords:
Hydrodynamic cavitation
Cavitation on a chip
Temperature effect
Microfluidics

ABSTRACT

This study presents an experimental investigation on the effects of the fluid temperature on hydrodynamic cavitation (HC) inside microfluidic devices (HC reactors) with multiple parallel microchannels. Three different reactors featuring microchannel configurations with hydraulic diameters of 89, 66, and 48 micrometers including 9, 21, and 37 microchannels respectively, were fabricated using the semiconductor-based microfabrication techniques. The microchannels have side wall roughness elements with a length of one-third of the entire microchannel length and a height of one-tenth of the hydraulic diameter. The fabricated HC reactors enable the investigation of cavitating flows under different thermophysical conditions at operating pressures ranging from 1.7 to 4.1 MPa and fluid temperatures at 23 °C, 33 °C, and 43 °C, and allow the observation of different cavitating flow morphologies, e.g., sheet, shear, and cloud cavities. According to the results, an increase in the temperature by 10 °C significantly raised the cavitation intensity. Furthermore, the scale effects amplify the effect of the temperature changes. Accordingly, the effect of the temperature is more dominant on the microscale compared to macroscale. An increase in the fluid temperature from 23 °C to 33 °C can double the cavitation penetration length in some microchannels within Reactor 1 at an upstream pressure of 3 MPa. The average penetration length at the extension region also increases (by approximately 70 % for Reactor 1, 50 % for Reactor 2, and 35 % for Reactor 3) upon change in the fluid temperature. The change in the cavitation intensity was larger for the temperature increase from 23 °C to 33 °C than for the increase from 33 °C to 43 °C which emphasizes the increasing dominance of thermal effects with temperature. This study offers understanding how a change in thermal properties influences HC at the microscale. The findings of this study can be utilized for scaling efforts in various applications relying on cavitation such as water treatment, microreactors, nanomaterial synthesis, and micro mixing.

1. Introduction

Cavitation is a phase change phenomenon that happens when the static pressure in a fluid flow falls below its saturation vapor pressure. The subsequent pressure rise along the flow leads to the collapse of small vapor-filled bubbles/cavities which results in a significant energy release to the surrounding area. This energy appears inside localized hot spots with temperatures and pressures as high as 5000 K and 500 atm, respectively [1,2]. Cavitation occurs in a wide range of cases from hydraulic machinery to biotechnology and biomedical applications, including the production of biofuels [3], synthesis of materials [4], brewing of beer [5], and wastewater treatment [6].

Microfluidic devices have emerged as an outstanding platform in the study of microscale fluid dynamics, which offers unique possibilities for conducting experiments that would have been difficult to accomplish on a larger scale such as high elasticity and low Reynolds number flows [7], inertial microfluidics [8], drug delivery and diagnostic devices [9]. Notably, local pressure drops measurements have convincingly validated the classical Navier-Stokes equations, even for channels as small as 4.5 micrometers in the height where Knudsen number is small enough

* Corresponding authors at: Faculty of Engineering and Natural Sciences, Sabanci University, 34956 Tuzla, Istanbul, Turkey.
E-mail addresses: morteza.ghorbani@sabanciuniv.edu (M. Ghorbani), kosara@sabanciuniv.edu (A. Koşar).

https://doi.org/10.1016/j.ijft.2025.101185

Available online 19 March 2025
2666-2027/© 2025 The Author(s). Published by Elsevier Ltd. This is an open access article under the CC BY-NC license (http://creativecommons.org/licenses/by-nc/4.0/).

to assume continuum mechanics [10,11]. However, multiphase flows were reported to have different behavior on the microscale when compared to conventional scale multiphase flows [12,13]. In this regard, significant differences between microscale and conventional scale cavitating flows were revealed in the literature [14,15].

Although there is no clear definition for cavitation intensity, it is typically assessed by considering parameters such as the size and shape of cavities [16,17]. In addition, the effectiveness, treatment ratio, and economic efficiency are other indirect but important parameters [2,18,19]. For instance, multiple studies repeatedly emphasized that the generation of facile cavitating flows could have a significant impact on water treatment, erosion rates, and other related processes [20–24]. Alongside the cavitation intensity, various factors including the intake pressure, pH levels, gas content, reagent concentration, working fluid, and duration of the treatment play a significant role [25–27].

Major thermophysical properties such as density, viscosity, vapor pressure [2], thermal conductivity [28], heat capacity, and latent heat [29] influence the generation and collapse of cavitation bubbles. For instance, higher thermal conductivity of lighter noble gases causes more thermal dissipation during the bubble collapse, leading to a lower peak temperature [28]. Variations in the fluid temperature alter these properties which affect the morphology of cavitating flows. At lower scales, due to higher surface to volume ratios, the significance of the surface tension and viscous effects grow. The thermal diffusion, heat transfer rate and energy dissipation vary accordingly which affects the stability and behavior of cavitation bubbles.

Most studies on HC have neglected the effects of the working fluid temperature and have assumed isothermal conditions instead, which might not be suitable for cryogenic fluids or hot fluids. Hot water has a more pronounced temperature-saturation pressure relationship with a steeper curve and lower liquid-vapor density ratios compared to cold water. As a result, during bubble growth, latent heat becomes essential to sustain a similar vapor cavity size. Additionally, the evaporative cooling effect substantially reduces the temperature in the liquid around the locations of cavitation, which corresponds to several degrees lower than the bulk temperature of the surrounding liquid [30,31] and emphasizes on the importance of thermal effects in understanding the cavitation phenomenon. In a related study, Petkovsek et al. [22] used the high-speed IR thermography method to investigate real-time fluctuations in the temperature and explore erosion caused by cavitation at water temperatures ranging from 30 °C to 100 °C. Their findings revealed a strong correlation between the cavitation intensity and temperature. The largest erosion rate was observed at approximately 60 °C in their study. Iga et al. [32] investigated how elevated water temperatures influenced cavitation behavior on a NACA0015 hydrofoil. They conducted experiments within a temperature range from 20 °C to 140 °C and observed that at 140 °C, the cavity length was consistently shorter than that at 20 °C for all cavitation patterns, indicating a significant thermodynamic suppression effect at higher temperatures. Additionally, temperature measurements inside the cavities revealed a reduction of approximately 0.3 °C at 80 °C and 0.05 °C at 20 °C under supercavitation conditions. Cervone et al. [33] investigated the influence of the temperature on cavitation by conducting experiments at three distinct water temperatures: 25 °C, 50 °C, and 70 °C. By keeping the cavitation number and flow speed fixed, they found that the longest-lasting attached cavity occurred at a temperature of 70 °C. In another study, Zheng et al. [34] investigated the temperature effect on the hydrodynamic characteristics of Rotational Super cavitating Evaporator (RSCE) by visualizing the cavitating flows at different water temperatures in RSCE under different rotational speeds. Their result suggested that the thermodynamic effect of cavitation was not significant at temperatures below 60 °C. Only slight changes were observed in the incipient cavitation number, which requires further investigations. In the study of Chen et al. [29], thermal effects were found to significantly alter cavitation behavior. Evaporative cooling within the cavity lowers the local temperature and saturation vapor pressure, which in turn increases the local cavitation number and results in a shorter, less developed cavity on a hydrofoil.

Although there have been extensive research efforts on cavitation, the impact of the working fluid temperature on this phenomenon was not considered at the microscale. Few studies, which were devoted to temperature effects on cavitating flow patterns, are available at the macroscale, where the surface tension and surface area-to-volume ratio are not dominant compared to inertial forces [35,36]. The recent investigations at the microscale illustrated that the cavitating flow patterns at this scale are different compared to macroscale [26,37,38]. The chemical effects which are the direct outcome of the thermal effects as a result of the cavitation bubble collapse are more intense at the microscale as well [39]. This suggests that the temperature effects of the working fluid could be influential at the microscale. In addition, the interactions between the fluid and boundaries at the microscale could affect the velocity profile and flow resistance [40]. The area-to-volume ratio also makes the effect of viscous forces important at the microscale. The concept of “HC on a chip” which has been introduced as a suitable platform for local HC investigations inside the microfluidic devices [41] could be taken into account in comprehensive parametric studies on HC at the microscale. In this study, we investigated the effect of working fluid temperature on cavitating flows and cavitation intensity at the microscale. The penetration length and void fraction were considered as the intensity parameters. The effect of temperature variations on the inception and characteristics of cavitating flows inside microfluidic devices housing multiple parallel microchannels were investigated where velocity profiles also affected the cavitation intensity in different areas of the cavitation on a chip according to its geometry and flow conditions. These findings could present valuable guidelines for designing efficient HC reactors to be used in many applications including chemical processes, medical devices, and energy systems. Our study will thus help in optimizing operating conditions for these applications by examining the temperature effect at the microscale which could trigger advances in the design and operation of HC reactors as well as microfluidic devices involving HC.

2. Methods and materials

2.1. Experimental setup

Fig. 1 presents a schematic of the experimental test rig used for the generation of cavitating flow patterns at different temperatures. For this, three different microfluidic devices (HC reactors) with different hydraulic diameters (D_h) of 48 μm, 66 μm, 89 μm were designed and fabricated using the standard microfabrication techniques. The reactors consist of an inlet port and inlet channel, microchannels, two ports for pressure measurement, and an open end for flow to discharge. Two ports were also considered as the outlet ports to ensure the reactor functionality in the closed end situation. A sandwich holder, which houses the reactors, enables all the ports to be closed when they are not needed. The details of the reactor dimensions are provided in Table 1. Roughness elements are designed as triangular geometries to be fabricated by means of electron beam lithography and dry etching. Roughness elements play a key role in increasing nucleation sites for cavitation bubbles which can lead to more frequent bubble formation [26,42]. The total length of roughness elements covers one third of microchannel length since our previous studies proved a substantial effect on cavitation intensity for these roughness configurations [26]. Hydrodynamic diameters were also selected and varied based on our previous studies, where it was 66 μm, to account for the effect of geometry and multiple channels on facile cavitating flow generation [38,41]. All the HC reactors include multiple parallel microchannels with different microchannel sizes and numbers. It was made sure that the total cross section area was equal for all the three reactors. The fabrication process flow of the HC reactors is presented in Fig. 2. A 2μm thick photoresist of ECI 3007 was used to pattern channels and ports on a 525 μm silicon wafer

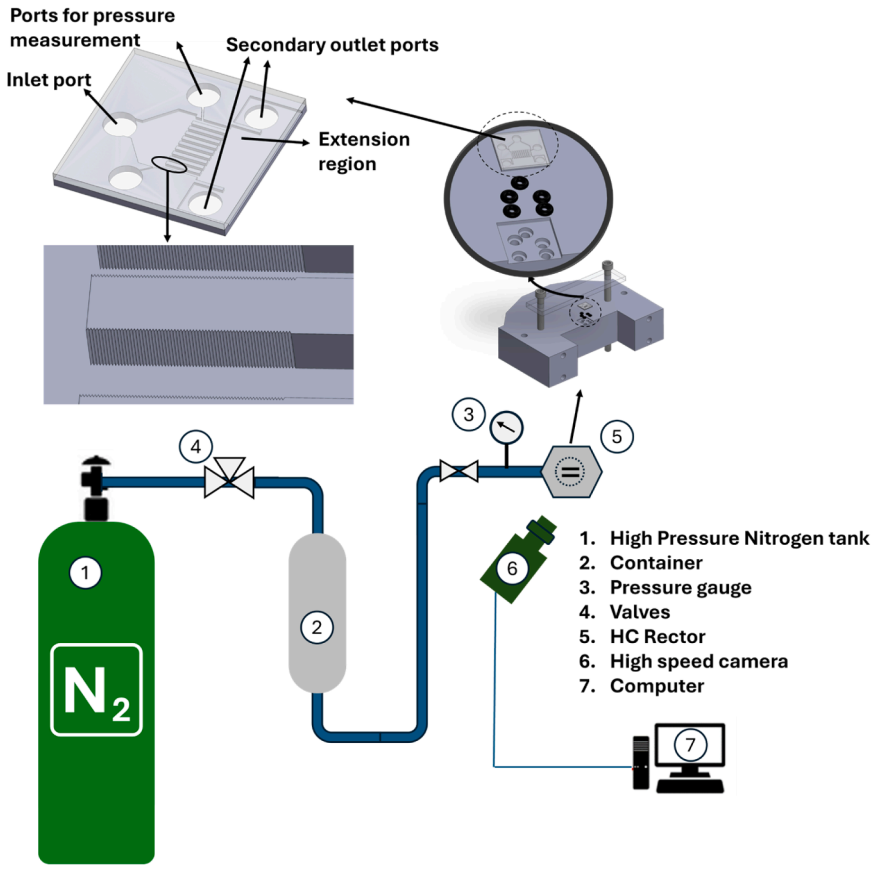


Fig. 1. Experimental setup for flow visualization including nitrogen tank, containers, HC reactor, and high-speed camera.

Table 1
Device dimensions.

	Reactor 1	Reactor 2	Reactor 3
Width of microchannels (μm) (W)	172	75	40
Hydraulic diameter (μm) (D_H)	89	66	48
Length of microchannels (μm) (L)	2000	2000	2000
Depth of microchannels (μm) (D)	60	60	60
Number of microchannels (N)	9	21	37
Roughness elements height (μm) (R_h)	8.9	6.6	4.8
Number of roughness elements	75	101	139
Length of extension region	2000	2000	2000

(Fig. 2.b). Then 500 nm SiO2 layer was dry etched using SPTS Advanced Plasma System machine (Fig. 2.c). A 10 nm layer of Titanium and a 1 μm layer of Aluminum were sputtered on the backside of wafers by DP650 magnetron sputtering machine to protect wafers against stress (Fig. 2.d). Afterwards, 500 nm of ZEP 520A EB resist was used for EBL process to etch the sidewall roughness elements which are in small triangular shapes (Fig. 2.e and f). Another 475 μm etching of silicon layer of only ports was performed using AZ 10XT-60 resist and SPTS Rapier etching machine (Fig. 2.g and h). Next, the whole pattern including ports, channels and roughness elements was etched for 60 μm using AZ 10XT-60 resist and SPTS Rapier etching machine to shape the final design on wafer (Fig. 2.i). After removing Al and Ti protective layers and SiO2 layers by wet etching (Fig. 2.j and k) and cleaning wafer using the Piranha solution, anodic bonding of front glass on silicon was performed by SB6 machine (Fig. 2.l). More details on fabrication process could be found in our previous studies [26,38].

The experimental test rig consists of components including a high-pressure nitrogen tank (Linde Gas, Gebze, Kocaeli), a liquid container (Swagelok, Solon, Ohio, US), appropriate tubing (Swagelok, Solon, Ohio, US), 2 μm particle filter (Swagelok, Solon, Ohio, US) and fine control valves (Swagelok, Solon, Ohio, US). A pressure gauge (Omega, USA) with an accuracy of ±0.25 % and a range of up to 3000 psi was installed on the flow path downstream of the nitrogen tank exit to measure the upstream pressures. A homemade holder made of aluminum was designed and fabricated to enclose the HC reactors. To ensure a leak-proof system, silicone O-rings were employed as effective sealing components between the HC reactor and holder. The fluid temperature was measured by means of a thermocouple (Omega, USA) and a thermometer installed before the entrance of the particle filter (Uni-Trend Technology, China).

2.2. Experimental Procedure

Deionized water at three different temperatures, namely, ambient temperature (23 °C), 33 °C, and 43 °C, was introduced into the container. Using the fixed upstream pressure, which was supplied by the nitrogen tank, the liquid was pushed into the HC reactor from the top of the tank at upstream pressures from 1.7 MPa to 4.1 MPa, exiting as a jet flow to the ambience after passing through the reactor, and was visualized by the high-speed camera at the same time. The upstream pressures were chosen to allow inception, developed flow, and supercavitation conditions for water at ambient temperature, while considering the structural integrity of the reactors. A particle filtering valve (Swagelok, Solon, Ohio, US) was used to obstruct the flow of particles larger than 2 micrometers into the reactor. The dissolved N_2 content was not directly measured, but the same batch of deionized water was used for all experiments. At 33 °C, water typically contains about 20 mg/L of N_2 at 1 atm. Using the Henry's law ($C = k_h \cdot p$), where k_h is approximately 20 mg/(L·atm) for N_2 at room temperature, the equilibrium concentration can be obtained as:

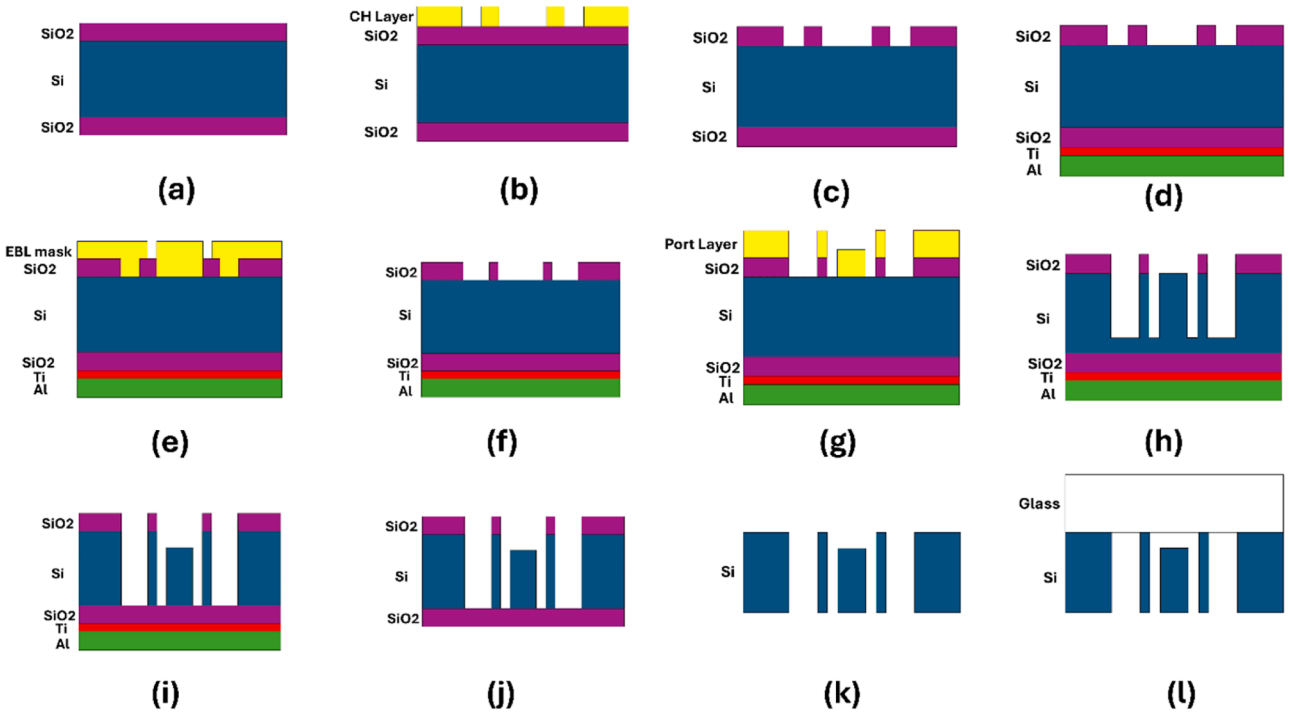


Fig. 2. Process flow for microfabrication. (a) SiO_2 coating. (b) Patterning channels and ports using lithography. (c) Dry etching. (d) Sputtering of Ti and Al. (e) Electron beam lithography for patterning roughness elements. (f) Dry etching. (g) Patterning port layers. (h) Dry etching. (i) Dry etching of whole patterns to shape the full device. (j) Wet etching of Al and Ti. (k) Wet etching of SiO_2 layer. (l) Anodic bonding.

- At 1.7 MPa: 20 mg/L × 17 ≈ 340 mg/L
- At 4.1 MPa: 20 mg/L × 41 ≈ 820 mg/L

At 43 °C, these values would be slightly lower due to decreased N_2 solubility with increasing temperature. However, the pressurization step lasts for less than 10 s, and using the diffusion coefficient for N_2 in water (~2×10^{-9} m^2/s), the diffusion depth for 10 s can be calculated as:

$$\sqrt{2 \cdot D \cdot t} = \sqrt{2 \times 2 \times 10^{-9} m^2/s \times 2s} \approx 200 \mu m$$

This means that a thin layer near the interface can approach these high-pressure equilibrium values. Consequently, the variation in the dissolved N_2 content due to the upstream pressure (and the slight temperature differences between 33 °C and 43 °C) is minimal, and it is unlikely to significantly affect the bubble nucleation behavior under our experimental conditions. The mean flow velocity inside microchannels, v_{ref} (m/s), was calculated using the flow rate, size of channels, and number of channels as:

$$v_{ref} = \frac{V}{6 \times 10^{-5} \times W \times N \times t} \quad (1)$$

where

V is the volume of the fluid passed through channels within time t (incubicmeters),

W denotes the width of channels (in meters),

N represents the number of channels, and t is the time over which the volume is measured (in seconds).

Flow parameters are provided in Table 2.

At the microscale, the surface tension which decreases with the inlet temperature becomes a significant parameter in the formation and development of cavitating flows [43–45]. The surface tension of water is 0.07232 N/m at 23 °C, whereas it is 0.07072 N/m and 0.06909 N/m at 33 °C and 43 °C, respectively. Sidewall roughness elements with a length of one third of the entire microchannel length and a height of 0.1 D_h were selected for all the reactors in parallel lines with our previous studies [26], where intense cavitation was achieved. The cavitation number (σ) serves as a dimensionless number in characterizing the cavitation phenomenon:

Table 2
Flow parameters at each temperature and upstream pressure for Reactor 1.

Temperature	Upstream Pressure (MPa)	Flow rate (ml/s)	Mean velocity (m/s)
23 °C	1.7	2.631	27.85
	2.4	3.125	33.07
	3	3.571	37.79
	3.4	4	42.33
	4.1	4.651	49.22
33 °C	1.7	2.663	28.18
	2.4	3.159	33.43
	3	3.61	38.2
	3.4	4.04	42.75
	4.1	4.684	49.56
43 °C	1.7	2.702	28.6
	2.4	3.226	34.1
	3	3.636	38.48
	3.4	4.082	43.18
	4.1	4.762	50.39

$$\sigma = \frac{P - P_v}{\frac{1}{2}\rho v_{ref}^2} \quad (2)$$

where P is the upstream pressure (Pa), P_v is the saturation vapor pressure of the liquid (Pa) which varies from 2812 Pa at 23 °C to 5036 Pa at 33 °C and 8651 Pa at 43 °C for water, and ρ is the liquid density (kg/m^3). Low values of cavitation number suggest more intense cavitation [26,46].

The Reynolds (Re) number, which represents the ratio of inertial forces to viscous forces, is expressed as:

$$Re = \frac{\rho v_{ref} D_h}{\mu} \quad (3)$$

where μ is the dynamic viscosity of the fluid.

The Weber number (We) is another dimensionless number and

relates the fluid inertia to its surface tension:

$$We = \frac{\rho v_{ref}^2 D_h}{\gamma} \tag{4}$$

where γ is the surface tension (N/m).

2.3. HC visualization and post-processing methodology

Cavitating flows inside the microchannels and extension region of HC reactors were recorded via a high-speed camera (Phantom VEO-710) equipped with a double-shutter CMOS sensor and an 8X lens. Images were acquired at 5000 fps for a resolution of 1280 × 800 pixels and exposure time of 200 μs. A cold light halogen source (SOIF 5100-L) was used to illuminate the cavitating flow patterns during recording. The acquired images were then analyzed to evaluate the void fraction within the cavitation regions. To enhance the clarity and contrast of images, image processing was utilized using Python programming language. Each image was rescaled in terms of the light intensity, setting the value of the darkest pixels to 0 and the brightest pixels to 1. Then, the average value corresponding to the void fraction for each channel exit zone was calculated as:

$$I_{ave} = \frac{\sum \left(1 - \frac{I_i}{255}\right)}{N_p} \tag{5}$$

where I_i represents the intensity of each pixel, and N_p is the total number of pixels.

Rescaling was applied to grayscale 8-bit images, where each pixel can represent 256 different shades of gray. This normalization of pixel values displays the contrast between the cases of cavitation and absence of cavitation, thereby allowing us to estimate the void fraction. However, it should be mentioned that this method provides an approximate value rather than a direct quantitative measurement of void fraction. The extraction of void fraction from shadowgraphy images introduces several sources of uncertainty. One major factor is the variability in halogen illumination, which can fluctuate both spatially and temporally depending on the light source's position and distance from the camera, affecting the consistency of image brightness. Additionally, optical effects, such as diffraction, scattering, and refraction around cavitation bubbles, can distort the image, making the inner part of the bubble appear darker while the edges are lighter, which may be misinterpreted as liquid. The inaccuracies in the linear mapping of grayscale values to void fraction also contribute to the uncertainty since the relationship between image brightness and void fraction is not straightforward or perfectly linear. Furthermore, image processing techniques such as thresholding can introduce additional errors, especially when the contrast between bubble regions is subtle. Thus, while the method provides a useful trend and approximate values, the extracted void fraction should be interpreted with caution given these multiple sources of uncertainty.

Table 3 represents the uncertainties in experimental parameters which were obtained from manufacturers datasheets or by using the uncertainty propagation method [47].

Table 3
Uncertainties in major parameters.

Uncertainty	Error (%)
Cavitation Number	±9.1
Reynolds Number	±6.69
Weber Number	±9.24
Flow rate	±1.7
Penetration Length	±7.93

3. Results

The experiments on three different HC reactors were conducted at upstream pressures ranging from 1.7 MPa to 4.1 MPa and at three different temperatures, namely, ambient temperature (23 °C), 33 °C, and 43 °C to identify pressure-driven cavitating flow patterns of DI water.

3.1. Characterization of HC reactors at room temperature

3.1.1. The evolution of cavitating flow patterns

Fig. 4 displays the inception and development of cavitating flows inside the microchannels of Reactor 1 with respect to the upstream pressure at room temperature, while Fig. 5 shows the extension region of Reactor 1. The results show that cavitation inception occurs in both microchannel and extension region at the upstream pressure of 2.4 MPa (σ = 4.41) for this reactor. It should be noted that cavitation incepts in microchannel number 1, which is located 1376 μm above the center of the reactor in the form of a sheet cavity, while no cavitation is observed in the other microchannels.

Furthermore, shear cavities, which form when the velocity of fluid layers differ due to high shear rates and create a velocity gradient followed by pressure drop [48,49], can be observed as parallel twin cavities and single cavity patterns at different locations of the extension. Single cavities are observed to emerge with frequencies of approximately 1700 Hz (which was calculated according to incidence and timeframe of the high-speed camera). Furthermore, they appear 200 μm away from the tip located between the outlet of microchannels 1 and 2 as well as microchannels 2 and 3 at the extension region. Twin cavities form in the extension regions between outlets of channels 3 to 8, while there is an absence of cavitating flow between outlets of channels 8 and 9. To further quantify the shedding dynamics, we used Strouhal number which is defined as:

$$St = \frac{fL}{V} \tag{6}$$

where f is the vortex shedding frequency, L is a characteristic length of the device, and V is the flow velocity. This dimensionless parameter normalizes the shedding frequency relative to the system's scale and operating conditions, allowing for a consistent comparison of vortex shedding behavior for different devices and Reynolds numbers. As illustrated in Fig. 3, the St–Reynolds number trends for the three microfluidic devices are quite similar, with only minor variations attributable to geometric differences.

It should be noted that the frequency measurements—and consequently the calculated Strouhal numbers—are approximate. The high-speed imaging was performed with a 200 μs time interval, and the rapid shedding events occur over only 2–5 frames, which introduces some uncertainty in the absolute values.

Upon an increase in the pressure to 3 MPa (σ = 4.15), cavitation

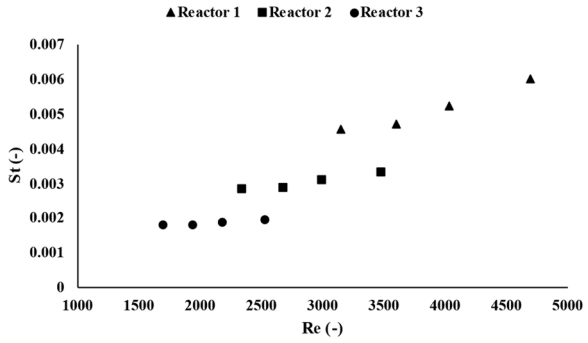


Fig. 3. Strouhal number of devices in different Reynolds numbers.

inception is observed in microchannels 2 and 9, with a similar pattern to microchannel 1 at the upstream pressure of 2.4 MPa (σ = 4.41). Furthermore, the pattern within microchannel 1 continues to shift to developing continuous thin form of cavities with re-entrant jet which form along the walls and are called sheet cavities. Re-entrant jet and vortex structure are believed to have a critical effect on breaking off cavities and formation of cloud cavities [50–52]. Sheet cavities void ratios can reach up to 50 % under certain conditions [53]. It is important to note that there is a certain degree of similarity in terms of flow patterns and penetration length between microchannels 1 and 9, which implies that the velocity profiles within these two locations should be similar.

The cavitating flow development can also be observed regarding the patterns at the extension region for the upstream pressure of 3 MPa (σ = 4.15) at which twin cavities get closer to the channel outlet wall compared to 2.4 MPa (σ = 4.41) (Fig. 5). Furthermore, single and twin cavities with frequencies similar to the pressure of 2.4 MPa (σ = 4.41) emerge between the outlet regions of microchannels 1 and 2 as well as of microchannels 8 and 9 at this upstream pressure. This suggests that the velocity at this region is sufficiently increased enough to lead to larger pressure drops and thus to favorable conditions for the formation of cavitation bubbles [54,55].

The intensity of the cavitating flow significantly increases at the pressure of 3.4 MPa (σ = 3.86), despite the relatively small increase in the pressure (from 3 MPa (σ = 4.15)). An increase in the pressure to 3.4 MPa (σ = 3.86) results in sheet cavities in other microchannels as shown in Fig. 4. Inception can be also seen in microchannel 8 at this pressure, and a recirculation area located near the lower surface of the developed cavity is evident inside microchannel 1. The recirculation area retains the stability of the sheet cavities by enabling the retention of vapor bubbles in the region for prolonged durations, thereby enhancing the size and thickness of the sheet [56,57].

Meanwhile, twin cavities continue to develop in the rest of the microchannel outlets in the extension region. The formation of these twin cavities starts shortly after the flow exits the microchannels, as depicted in Fig. 5. Upon an increase in the upstream pressure to 4.1 MPa (σ = 3.42), fully developed cavitation is achieved in microchannel 1 which extends to the outlet of this channel.

3.1.2. Effect of geometry on cavitating flows

The number of microchannels and their cross-section area were determined to ensure equal flow rates ranging from 2.63 mm^3/s for all reactors at upstream pressure from 1.7 MPa (σ = 4.44) to 4.65 mm^3/s at upstream pressure of 4.1 MPa (σ = 3.42) to maintain the same mean velocity conditions for all reactors. The results show that, under identical conditions, inception occurs earlier in larger microchannels which agree with the findings in the literature [26].

As can be seen in Fig. 6, cavitation incepts at 2.4 MPa (σ = 4.41) in the first microchannel of Reactor 1. Meanwhile, inception is detected inside the first microchannel of Reactor 2 at 3.4 MPa (σ = 3.86) with a penetration length of less than half of that for Reactor 1 at 2.4 MPa (σ = 4.41). For Reactor 3, cavitation is not visible in any channel at all the upstream pressures due to the very small nature of channels and shadow effects.

As can be observed in Fig. 4, cavitation inception and development happen in microchannels 1 and 9 at different upstream pressures, and eventually fully developed cavitation is reached in microchannel 1 in Reactor 1. Inception can be observed in microchannel 1 of Reactor 2 at the upstream pressure of 3.4 MPa (σ = 3.86). While development in microchannel 1 is not significant upon an increase in the pressure to 4.1 MPa (σ = 3.42), inception is observed in microchannels 2 and 3 at the upstream pressure of 4.1 MPa (σ = 3.86) (Fig. 6.c).

Fig. 7 shows the inception and developed cavities in the extension region of Reactor 2. Inception in the extension region occurs at the outlet of certain microchannels at the upstream pressure of 2.6 MPa with a maximum penetration length of 409 μm, which is shorter compared to the maximum value of 548 μm for Reactor 1 at 2.4 MPa (σ = 4.41), which reveals a delay in inception for Reactor 2. At the highest upstream pressure of 4.5 MPa, the maximum penetration length of developed cavities, which appear at the outlet of central microchannels, becomes

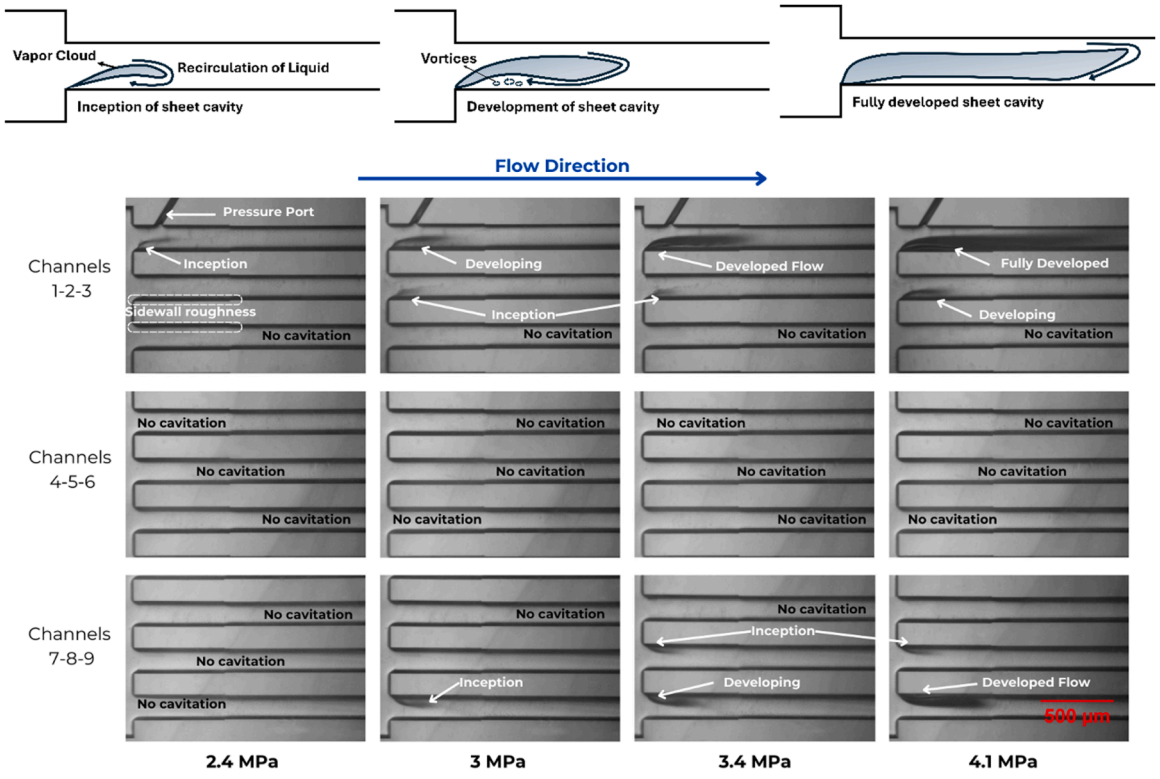


Fig. 4. Cavitating flow patterns inside microchannels for Reactor 1 at the temperature of 23 °C and different upstream pressures.

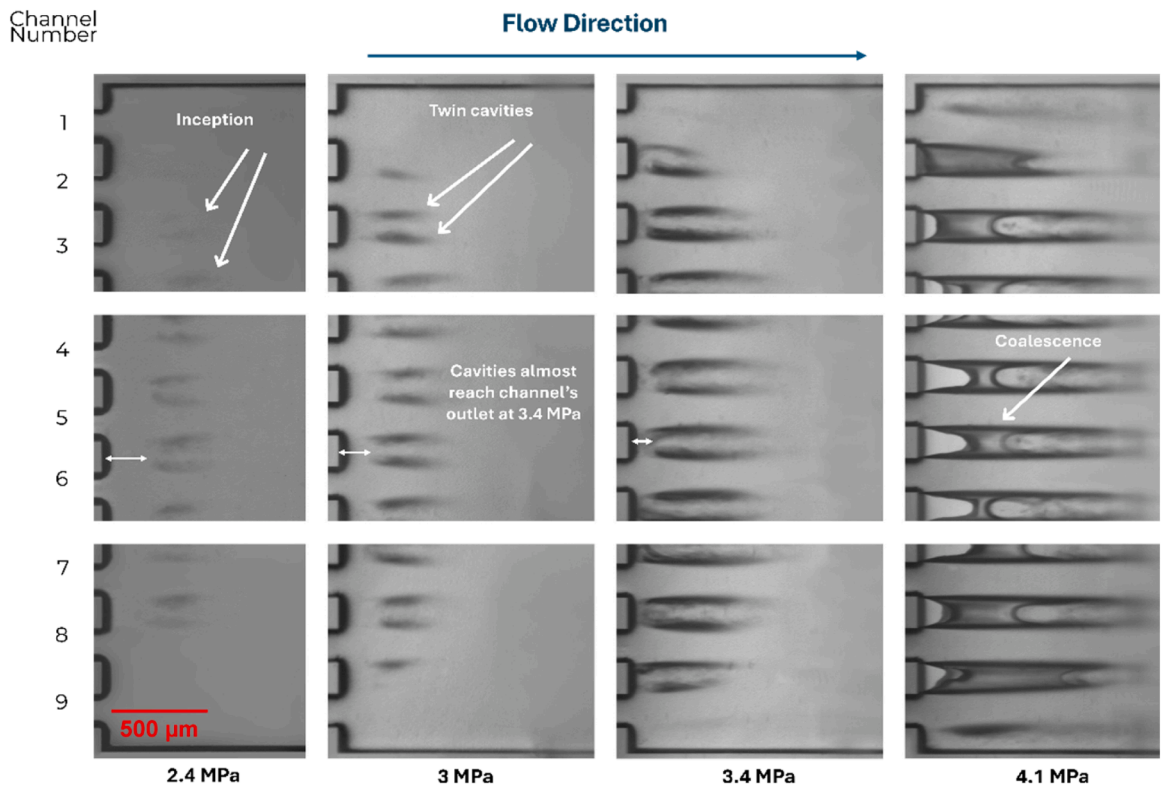


Fig. 5. Cavitating flow patterns at extension of Reactor 1 at the temperature of 23 °C and different upstream pressures.

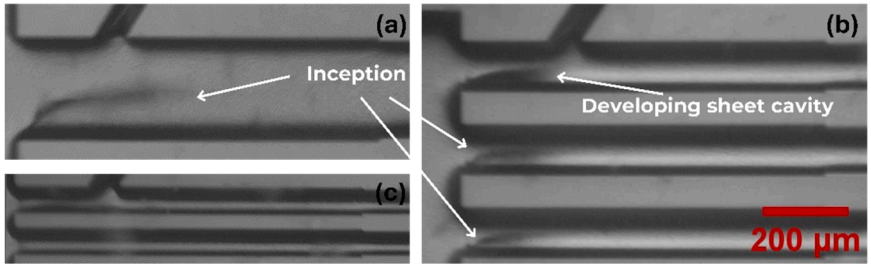


Fig. 6. Cavitation penetration in the microchannels of (a) Reactor 1 at 2.4 MPa (σ = 4.41). (b) Reactor 2 at 3.4 MPa (σ = 3.86) and (c) Reactor 3 at 4.1 MPa (σ = 3.42).

1097 µm for Reactor 2 which is less compared to 1200 µm for Reactor 1 at the upstream pressure of 4.1 MPa (σ = 3.42). This implies that by reducing the microchannels width from 172 µm to 75 µm while keeping the depth constant and decreasing the size of roughness elements from 8.9 µm to 6.6 µm, cavitation inception and development could be delayed.

By further reducing the size of the microchannel width from 75 µm to 40 µm at the same depth and decreasing the roughness element to 4.8 µm, developed cavities in the extension region at the upstream pressure of 3.4 MPa (σ = 3.86) become more intense with a maximum penetration length of 1279 µm for Reactor 3 (Fig. 8(a)) while the corresponding maximum length for Reactor 1 at the same pressure is 793 µm. The penetration length for Reactor 3 at upstream pressure of 3.4 MPa (σ = 3.86) which is 1279 µm is longer compared to Reactors 1 and 2 even at the upstream pressure of 4.1 MPa (σ = 3.42) with penetration lengths of 1200 µm and 1097 µm, respectively. Fig. 9 shows the penetration length at the extension for each Reactor at different distances from upper wall for the upstream pressure of 4.1 MPa (σ = 3.42).

3.2. Effect of the temperature of the working fluid on the cavitating flow development

In Figs. 10–12, high-speed images are displayed for different fluid temperatures in Reactor 1 under identical conditions, namely, approximately the same velocity and cavitation number. Cavitating flows in other reactors follow similar patterns. Fig. 10 displays flow patterns for microchannel 1 of Reactor 1. As previously mentioned, inception occurs at 2.4 MPa (σ = 4.41) (see Fig. 4) at room temperature. At the same pressure, a developing cavitating flow pattern can be observed for water at the temperature of 33 °C while inception occurs at the pressure of between 1.7 MPa (σ = 4.34) and 2.4 MPa (σ = 4.32) (Fig. 10.e). Inception also happens for water at 33 °C in an upstream pressure of 2.4 MPa (σ = 4.32) in microchannels number 2, 8, and 9, where cavitation cannot be seen at ambient temperature and at the upstream pressure of 2.4 MPa (σ = 4.41). While developing cavitating flow occurs at upstream pressure of 3 MPa (σ = 4.15) for water at room temperature, it can be observed that developing cavitating flow pattern at a lower pressure of 2.4 MPa (σ = 4.32) and at temperature of 33 °C is more intense than that of 23 °C at 3 MPa (σ = 4.15) (Fig. 10.c and e).

As the fluid temperature is increased by further 10 °C, cavitation

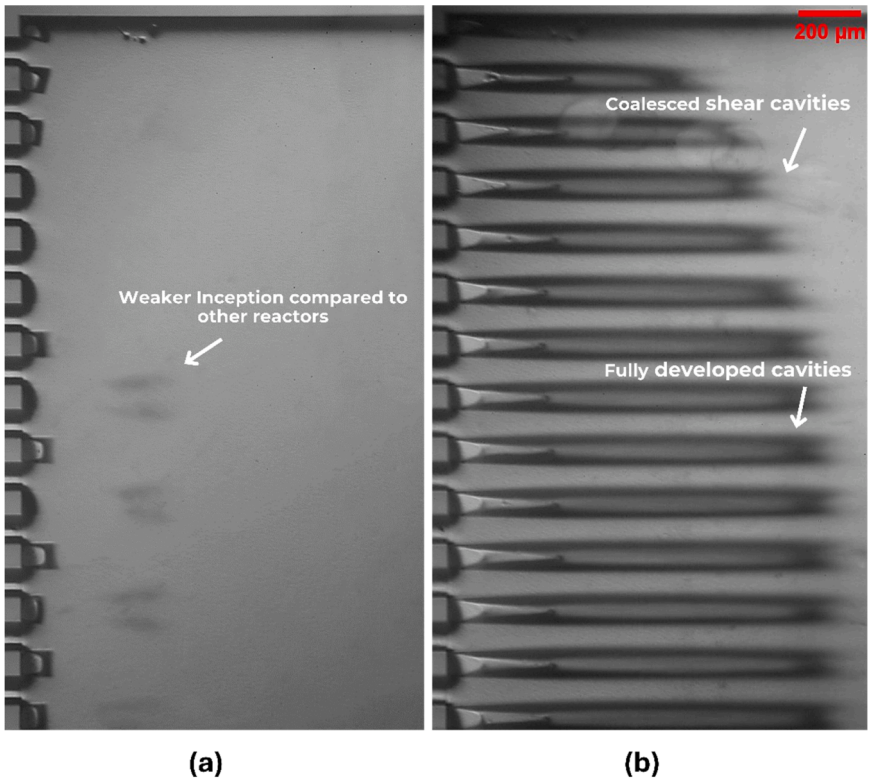


Fig. 7. (a) Cavitation inception at 2.4 MPa ($\sigma = 4.41$) and (b) developed cavities at the upstream pressure of 4.1 ($\sigma = 3.42$) for Reactor 2.

inception happens earlier. While there is no cavitation at pressure of 1.7 MPa at temperatures of 23 °C ($\sigma = 4.44$) and 33 °C ($\sigma = 4.34$), inception becomes visible for water at temperature of 43 °C at this upstream pressure ($\sigma = 4.22$) (Fig. 10.g). Meanwhile, no cavitation inception is observed for other microchannels at this pressure. Developed flow, which occurs for the water with the temperature of 23 °C at an upstream pressure of 3.4 MPa ($\sigma = 3.86$), can be observed with more intensity at 3 MPa for water at 33 °C ($\sigma = 4.07$) (Fig. 10.f). As the temperature is further raised to 43 °C, a similar pattern with more intensity can be seen at 2.4 MPa ($\sigma = 4.15$) (Fig. 10.h).

The fully developed flow for microchannel 1 at different temperatures (Fig. 11) shows that upon an increase in the temperature from 23 °C to 33 °C, the upstream pressure corresponding to a similar fully developed flow decreases substantially by 17.1 %, and the corresponding cavitation number increases by 9.6 %. This trend also exists when the temperature increases from 33 °C to 43 °C where an 11.8 % decrease in the upstream pressure, and a 6.06 % increase in the corresponding cavitation number is obtained to reach almost fully developed cavitation.

Similar to microchannels, inception happens earlier in the extension region at 33 °C compared to the ambient temperature in Reactor 1. Fig. 12.a displays more intense incipient cavitation in the region between outlets of microchannels 1 and 2 as twin cavity for water at the temperature of 33 °C and upstream pressure of 2.4 MPa ($\sigma = 4.32$) compared to water at 23 °C and the same upstream pressure ($\sigma = 4.41$) (shown in Fig. 5). Also, cavitating flow initiates in a region closer to the outlet compared to water at temperature of 23 °C. Similarly, the penetration length of developing twin cavities in middle regions of extension is longer compared to incipient cavitation for water at 23 °C (Figs. 12.a and 5). Upon an increase in the pressure for water at 33 °C to 3 MPa ($\sigma = 4.07$), developing cavities can be observed for all the regions between outlets with increasing length. Also, at this pressure, coalescence between twin cavities happens. Furthermore, cavitating flows tend to attach to the wall between the outlets of microchannels which suggest that shear cavities start to form intensely just at the exit of the microchannels (Fig. 12.b). Upon an increase in the pressure to 3.4 MPa at 33 °C ($\sigma = 3.79$), fully developed cavities become visible in the extension zone (Fig. 12.c).

A further increase in the temperature to 43 °C results in earlier cavitation inception in the extension region which happens at a decreased pressure of 1.7 MPa ($\sigma = 4.22$). Inception is observed in the region between outlets of microchannels 3 and 4 as well as of microchannels 4 and 5. Cavitation inception is not present at this pressure for water with temperatures of 23 °C and 33 °C. Developing cavities in the extension region are more intense for water at 43 °C and at the upstream pressure of 2.4 MPa ($\sigma = 4.15$) compared to water at 33 °C and at the same upstream pressure ($\sigma = 4.32$). Similarly, these cavities are observed to be closer to the outlet of microchannels (Fig. 12.a and e). Fully developed cavitating flow and coalescence can be seen at the pressure of 3 MPa for water at the temperature of 43 °C ($\sigma = 4.02$) where a similar pattern is observed at the upstream pressure of 3.4 MPa for water at the temperature of 33 °C and at the upstream pressure of 4.1 MPa for water at the temperature of 23 °C ($\sigma = 3.42$).

The cavity region depends on the intensity, which can be quantified by the cavity length, thickness, or area in 2D imaging. In this study, the cavity penetration length could be determined in the microchannels and extension region via imaging. Fig. 13 compares the penetration length in the extension region for Reactors at different pressures and water temperatures while Fig. 14 compares the average penetration length in all devices and temperature for the same cavitation numbers. It is evident that the effect of temperature becomes more dominant as the upstream pressure increases or as the cavitation number decreases. Additionally, there is no significant difference when comparing devices and temperature conditions, regardless of whether the comparison is based on consistent upstream pressures with varying cavitation numbers or consistent cavitation numbers with varying pressures for the three different temperatures.

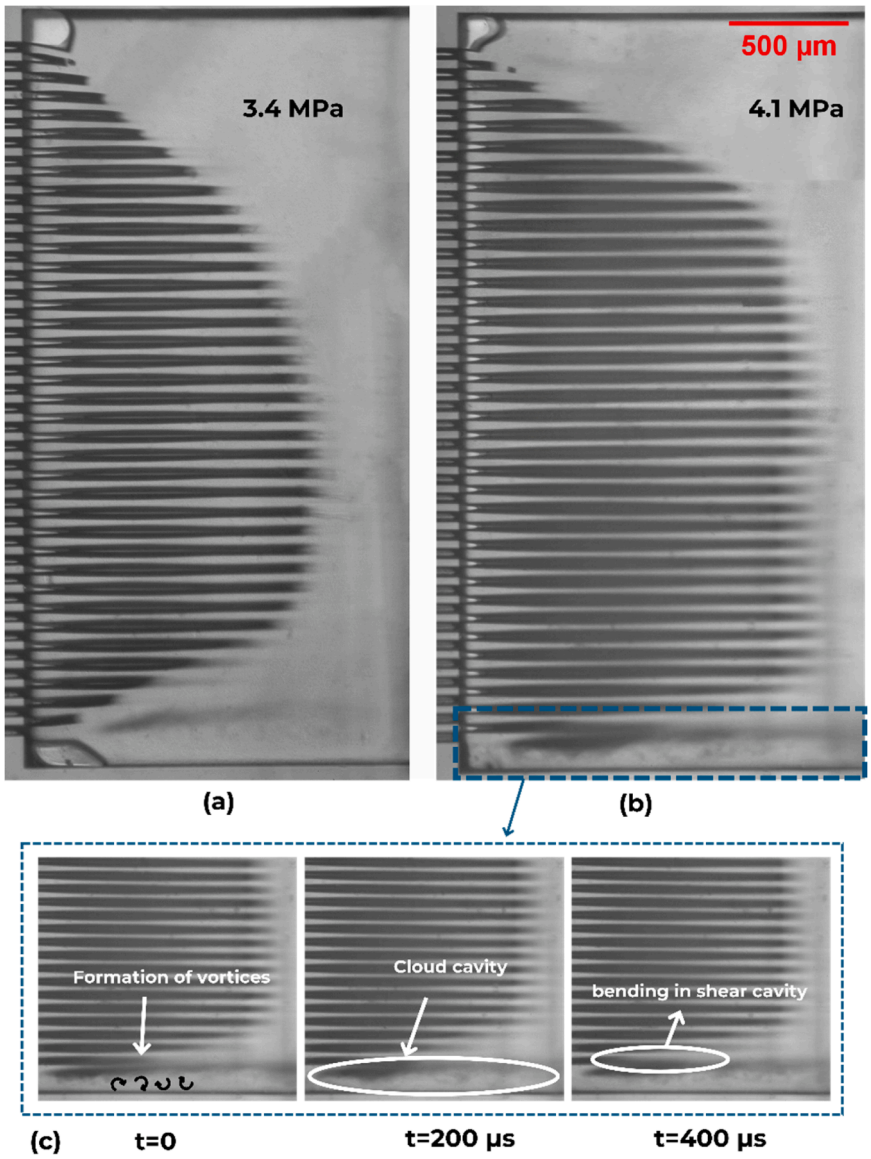


Fig. 8. Cavitating flow patterns at the upstream pressures of (a) 3.4 MPa ($\sigma = 3.86$) and (b) 4.1 MPa ($\sigma = 3.42$) of Reactor 3 and (c) cloud cavity behavior with time intervals of 200 µs.

4. Discussion

4.1. Cavitating flow patterns in multiple parallel microchannels

One of the cavitating flow patterns observed within the microchannel section is known as sheet cavitation, as depicted in Fig. 4. This specific cavitation pattern becomes visible initially at the edges of microchannels and manifests itself when there is a sudden change in the cross-sectional geometry. Under these circumstances, a recirculation zone generated by a viscous film which is called re-entrant jet emerges between the cavitating flow and solid body. This phenomenon occurs due to the interaction between the cavitating flow and solid structure. These conditions cause the formation of a region where the fluid circulates back on itself, creating a distinct recirculation zone at the interface between the cavitating flow and solid structure [51,53]

The earlier arrival of inception inside microchannels closer to the reactor walls suggests the presence of a larger vertical pressure gradient just before the microchannel entry. In addition, the existence of a vapor cloud that includes a recirculation area negatively influences the velocity gradient within these channels, leading to decreased velocities near their exit. The presence of higher velocities at the exit of microchannels located near the centerline, as indicated by earlier cavitation inception and development in the extension region of those microchannels (Fig. 5), confirms a subsequent higher reduction in the static pressure. The early onset of cavitation in the microchannels which happens at a lower upstream pressure and at a notably higher cavitation number is influenced by the specific geometry of the system which facilitates secondary currents where pressure gradients in curved streamlines push the bulk flow with lower velocities towards the center of the curvature and alter the flow velocity distribution, which in turn accelerates cavitation inception [58,59].

As the fully developed cavitating flow progresses downstream, it transforms into an oscillating cavitating flow known as shear cavitation, exhibiting dynamic fluctuations along its length (Fig. 8.c). At higher pressures, shear cavity at the outlet of microchannel 1 and the last microchannel is observed to transition to cloud cavity with shedding mechanism in all Reactors. This phenomenon can be clearly observed around the sidewall of the extension area in Fig. 5 and much more clearly for the lower sidewall of Reactor 3 (Fig. 8). The transition to cloud cavity is primarily governed by interactions within the fluid flow,

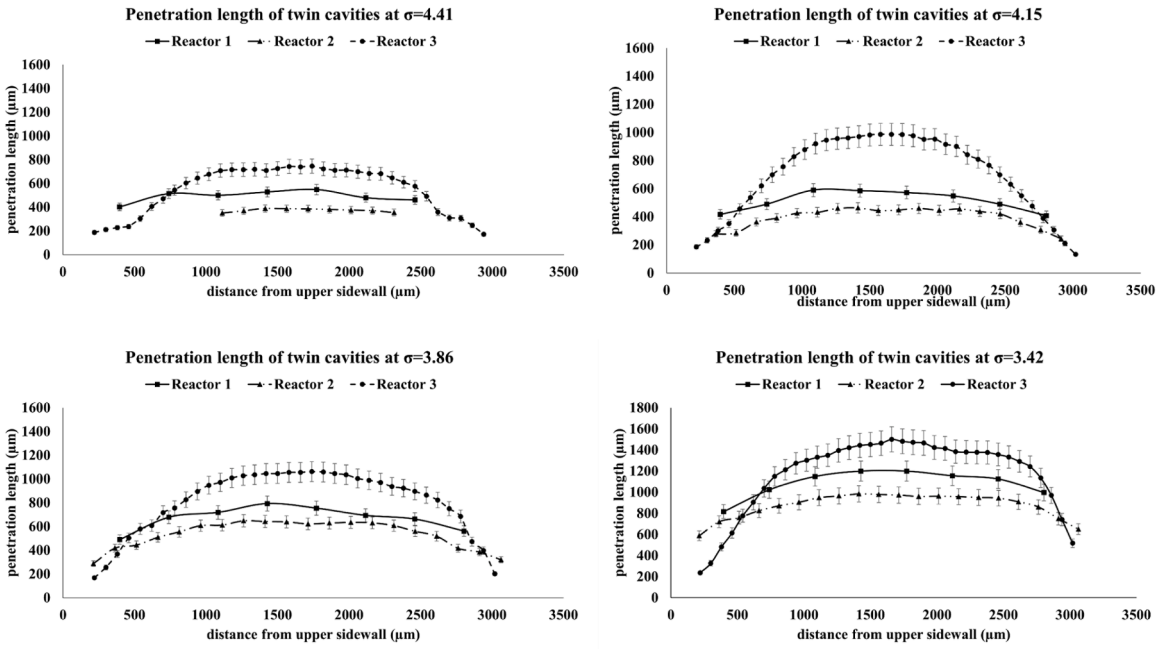


Fig. 9. Penetration length of twin cavities at different upstream pressures.

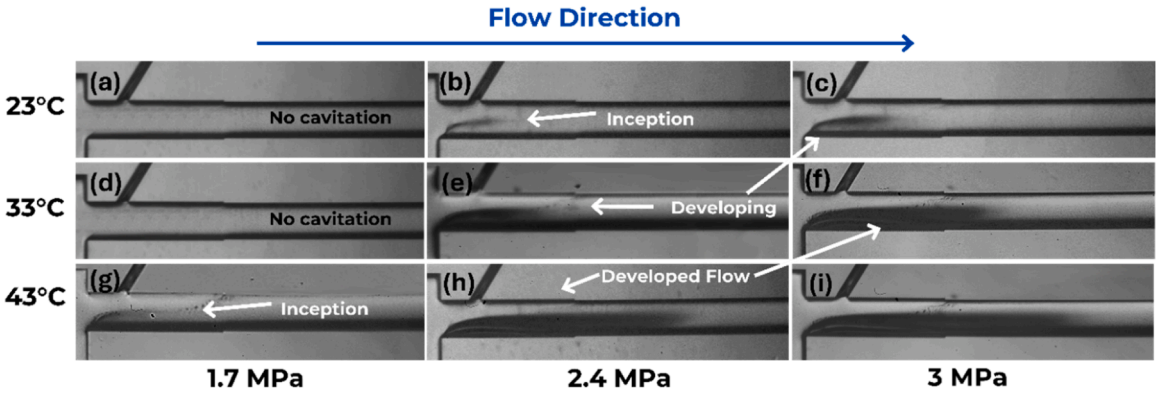


Fig. 10. Cavitation inception and development for microchannel 1 of Reactor 1 under different flow conditions (different fluid temperatures and pressures).

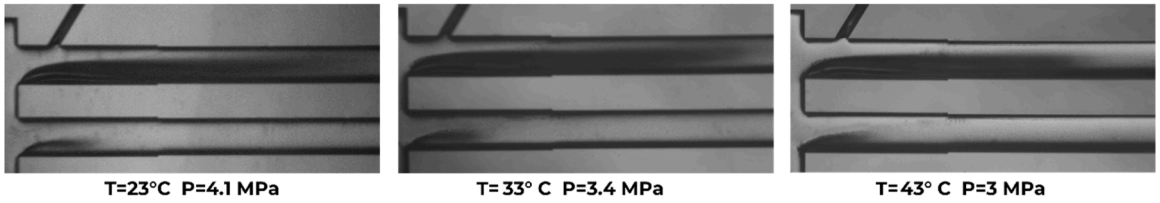


Fig. 11. Inlet pressures to reach fully developed cavitation for microchannel 1 of Reactor 1 at different fluid temperatures.

such as the growth of the shear cavity and motion of re-entrant jet. This jet moves backwards towards the origin of the cavity, and when it reaches a specific point, the transition occurs (Fig. 8). This phenomenon is characterized by the cavity length and penetration length of the re-entrant jet ratio, leading to the shedding of cavities [60,61].

4.2. Temperature role in microscale cavitating flow development

By maintaining a constant cavitation number during all the experiments, pressure differences could be obtained, allowing for the focus on temperature effects. As the temperature varies, it is crucial to assess both thermal and viscous effects. Specifically, as the temperature rises, the viscosity typically decreases, leading to an increase in the Reynolds number. Various models and parameters have been proposed to quantify these thermal effects on cavitation, demonstrating the complexity and importance of accurate assessment. The introduction of the thermodynamic parameter Σ (Equation 7) by Brennen [31] and its non-dimensional version Σ* (Equation 8) [62] are helpful in understanding how thermal effects influence cavitation. These parameters are critical for specifying the conditions under which vaporization and subsequent cavitation occur in various liquid environments. According to the Rayleigh-Plesset equation for the dynamics of a single spherical

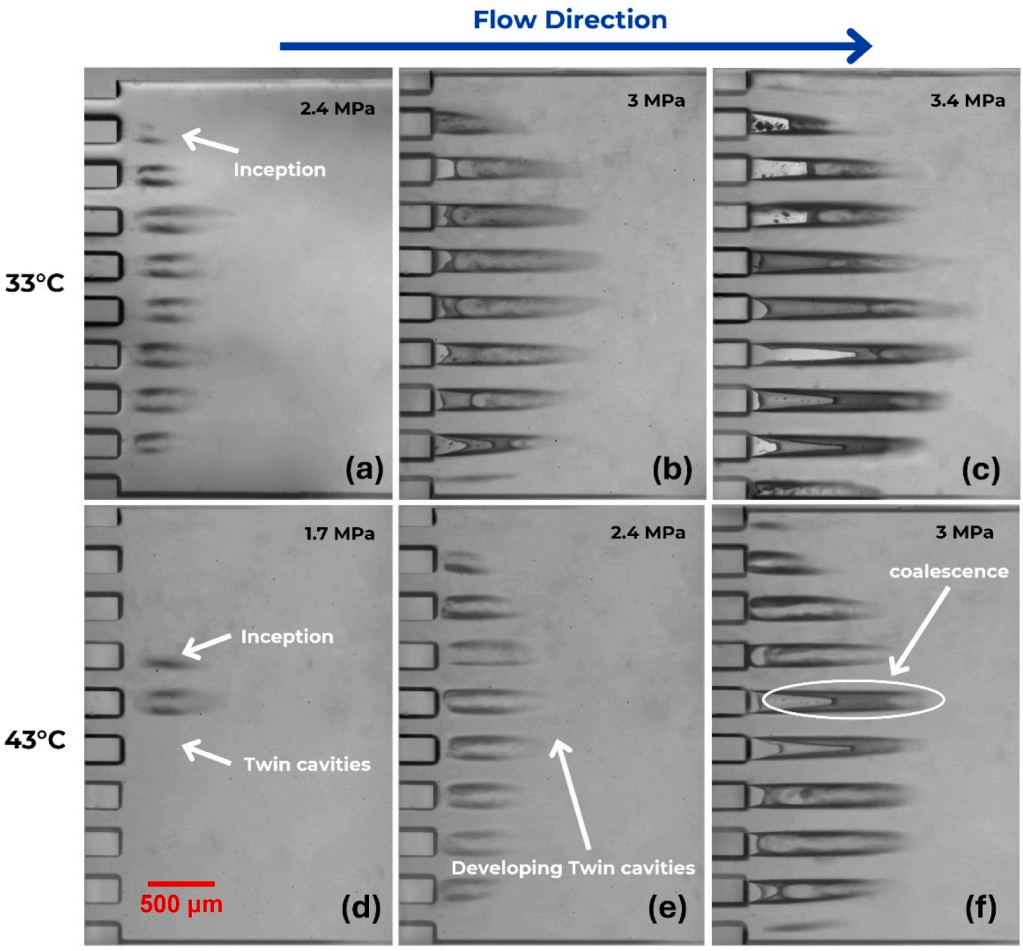


Fig. 12. Inception and development of cavitation under different flow conditions in the extension region of Reactor 1.

bubble, which takes the energy balance equation and heat diffusion equation into account, the thermodynamic parameter is critical for calculating the temperature change as the bubble diameter varies. This parameter is essential for determining the behavior of bubble dynamics [31]. Simulations using various advanced turbulent models have shown that both inertial and thermal effects contribute to the bubble growth in cavitation, particularly under cryogenic conditions where thermal effects are pronounced due to the substantial differences in vapor and liquid densities and latent heat of vaporization [63,64].

The thermodynamic parameter Σ and of its non-dimensional version Σ*are expressed as:

$$\Sigma = \frac{\rho_v{}^2 L^2}{\rho_l{}^2 c_{pl} T_\infty \sqrt{\alpha_l}} \tag{7}$$

$$\Sigma^* = \frac{\Sigma.\sqrt{H_{th}}}{\sqrt{U_{th}{}^3}} \tag{8}$$

where ρ_l represents the density of the liquid, α_l is the thermal diffusivity of the liquid, c_{pl} refers to the specific heat of water at constant pressure, ρ_v is the vapor density, L stands for the latent heat of vaporization, and T_∞ is the temperature of the liquid. H_{th} is the height of the channel, and U_{th} is the average flow velocity through the channel [65,66]. demonstrated that two thermally dominated flows could be considered as dynamically similar when Σ* is consistent for both cases. Typically, upon an increase in the fluid temperature, the thermodynamic parameter increases significantly due to a notable variation in ρ_v. To maintain the same cavity size, a higher vapor density implies decreased vaporization. As for the case of our study, upon an increase in the temperature from 23 °C to 33 °C, ρ_v increases from 0.0205 kg/m^3 to 0.034 kg/m^3 and reaches 0.0535 kg/m^3 at 43 °C while no significant changes are present for other properties (Table 4). This suggests that for a thermally dominated flow, an increase in the upstream pressure is required to maintain the same flow regime since the thermal effect could significantly act against cavitation.

Another mechanism that affects the cavitation bubble behavior at elevated temperatures is the viscous effect which predominates as the size decreases to microscale. As the viscosity decreases at elevated temperatures, Reynolds number increases [67,68] which is followed by an increase in the cavitation intensity. A model has been developed by Pelz et al. [60] to investigate the effect of Reynolds number on the velocity boundary layer of re-entrant jet and shedding. It was shown that for a constant cavitation number, the transition from sheet cavity to cloud cavity was evident upon an increase in Reynolds number. The results indicated that transition happened at lower Reynolds numbers for low cavitation numbers. According to the existing literature, there is a notable trade-off involving scale, working fluid, and temperature when assessing the thermal effects and viscous effects on cavitation, particularly as the temperature of the working fluid is altered. For instance, Franc et al. [62] on a four-bladed inducer who used the working fluid refrigerant R114 reported that at a similar cavitation number the cavitation length decreased significantly with the temperature which emphasizes the dominance of thermal effects over viscous effects.

The cavitation number for the cases of 3 MPa at 23 °C and 2.4 MPa at 43 °C are equal where the thermodynamic parameter significantly increases from 3 to 21, and Reynolds number increases from 3603 to 4865 in Reactor 1 which implies that inertial effects dominate over viscous

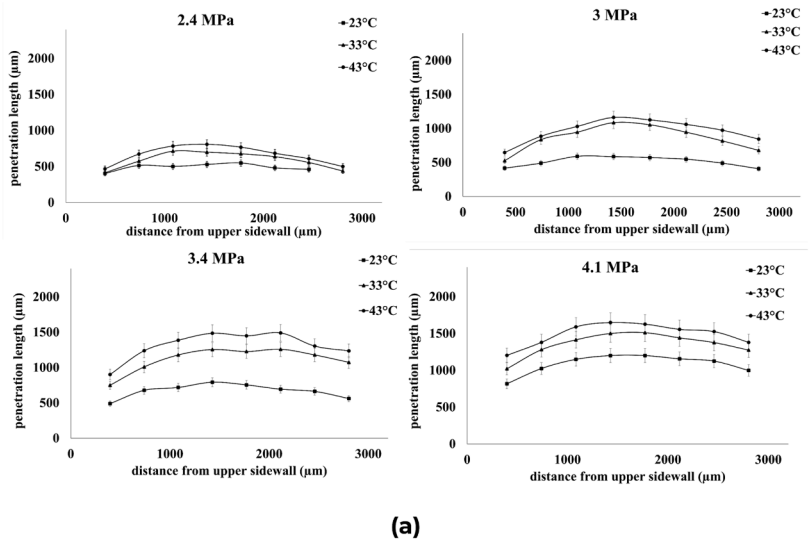


Fig. 13. Penetration length of cavitating flow at extension region of (a) Reactor 1 (b) Reactor 2, and (c) Reactor 3 under different flow conditions.

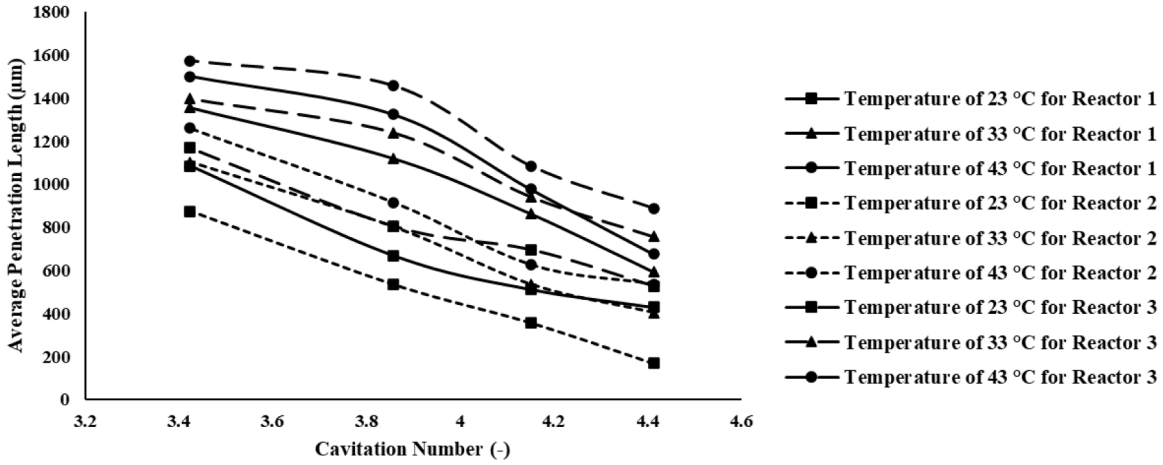


Fig. 14. Comparison of average penetration length in the extension region for reactors at different temperatures and constant cavitation numbers.

Table 4
Water properties for the different temperature conditions.

(K)	ρ_v (Kg/m^3)	$\rho_l(Kg/m^3)$	$c_{pl}J/Kg.K$	$\alpha_l(m^2/s)$	$L(KJ/Kg)$
296.15	0.0205	997.54	4180	0.000000143	2442
306.15	0.0205	997.54	4180	0.000000143	2442
316.15	0.0205	997.54	4180	0.000000143	2442

damping. The penetration length of cavitating flows for the 2nd case is longer, and the corresponding flow pattern is different. The surface tension decreases and influences rupture effects and subsequently the size of the bubbles and their lifespan. Lower viscosity also leads to an increase in cavitation activity because of weakening of molecular connections/bonds [69]. The experiments by Ge et al. [70] revealed that for water, the cavitation length increased with the temperature for temperature ranges similar to our work of study.

Surface tension, which decreases as the temperature rises, also affects the behavior of cavitating flow since it strongly influences rupture effects in fluid flow and thus the lifetime of bubbles as well as their size [15,71]. He et al [72] proposed a model which stated that a reduction in the surface tension resulted in bubbles with larger radius and delayed maximum temperature and maximum pressure.

Fig. 15 shows Reynolds and Weber numbers for different cavitation numbers for Reactor 1 while Fig. 16 displays the mean void fraction and thermodynamic parameter with respect to the upstream pressure. It is evident that upon an increase in the temperature a slight decrease in cavitation number occurs. At low cavitation numbers, an increase in the temperature has a significant impact on Reynolds number due to its impact on thermophysical properties such as the viscosity. Furthermore, a slight increase in Weber number could help in intensifying cavitation.

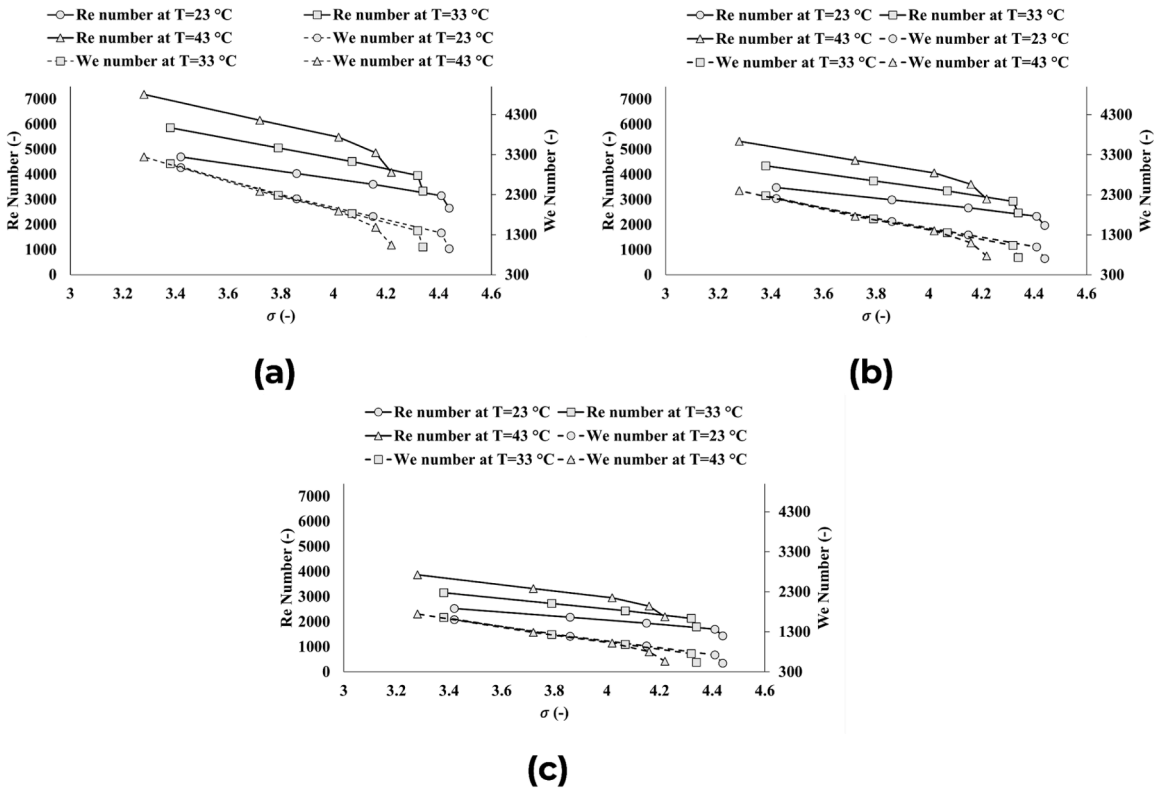


Fig. 15. Re and Weber numbers as a function of Cavitation number. (a) Rector 1 (b) Reactor 2 (c) Reactor 3.

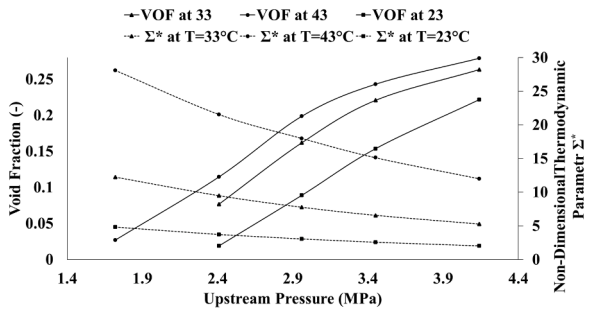


Fig. 16. Mean void fraction and non-dimensional thermodynamic parameter at different upstream pressures for Reactor 1.

At the microscale, the effect of surface tension becomes dominant which is the reason for an increase in cavitation intensity due to the decrease in surface tension upon an increase in fluid temperature. When comparing the cavitation penetration length increase in our study with the study conducted by [70] on the macroscale, it is evident that the increase in the cavitation length at the microscale is more for the same temperature increase. Upon an increase in the temperature from 23 °C to 33 °C cavitation, the length doubles for microchannel 1 at a cavitation number of 4.15 while there is a 70 % increase in the average penetration length in the extension region. At the same time, the increase in the cavitation penetration length for the venturi section at the macroscale was less than 25 % for all cavitation numbers ranging from 1.31 to 1.49 [70]. Even though an increase in the temperature to 33 °C and 43 °C raises the thermodynamic parameter which leads to delayed generation of bubbles, it is evident that viscous and surface tension effects are dominant over thermal effects in this temperature scale. Other studies in the literature investigating macroscale thermal effects reported that thermal phenomena dominate over viscous effects at an optimal temperature, with this dominance decreasing at temperatures both below and above this value [73].

5. Conclusion

In this study, the effects of the fluid temperature on cavitating flow regimes and intensity were investigated in three different microfluidic devices (Reactors) with parallel microchannels and roughness elements. Deionized water was used as the working fluid. Different flow patterns such as sheet cavity, shear cavity, twin cavity and cloud cavity were observed in Reactors with varying microchannel configurations. This study provides foundational knowledge for the design and optimization of HC reactors that offer a suitable platform for the use of various applications such as drug delivery, nanomaterial synthesis, and energy harvesting. The major conclusions from this study can be summarized as:

- The thermal and viscous effects can be regarded as the main parameters affecting the intensity of cavitation. An increase in the fluid temperature can lead to a rise in cavitation intensity or void fraction.
- The impact of the temperature increase is more pronounced at the microscale. An increase up to 70 % in mean cavity length at extension could be observed upon a change of 10^{o} C in the fluid temperature, which is more significant compared to macroscale results in the literature.
- The change in cavitation intensity is significantly larger for the temperature increase from 23 °C to 33 °C than from 33 °C to 43 °C which is attributed to larger viscous effects for the first case.

By manipulating the fluid temperature, emerging applications such as drug delivery systems, and nanomaterial synthesis could be realized [74,75]. Therefore, this study lays the groundwork for future research, which will aim at exploring the integration of HC reactors into complex systems, investigating other fluids to reveal the effect of fluid properties on cavitation dynamics, developing advanced numerical models, and further miniaturizing the device geometry to explore quantum effects in cavitation.

CRediT authorship contribution statement

Seyedreza Tebyani: Writing – original draft, Visualization, Validation, Software, Methodology, Investigation, Formal analysis, Data curation. **Farzad Rokhsar Talabazar:** Writing – review & editing, Writing – original draft, Visualization, Validation, Software, Methodology, Investigation, Formal analysis, Data curation. **Morteza Ghorbani:** Writing – review & editing, Writing – original draft, Supervision, Resources, Methodology, Investigation, Conceptualization. **Ali Koşar:** Writing – review & editing, Writing – original draft, Supervision, Resources, Project administration, Funding acquisition, Conceptualization.

Declaration of competing interest

The authors declare that they have no known competing financial interests or personal relationships that could have appeared to influence the work reported in this paper.

Acknowledgement

This work was supported by TUBITAK (The Scientific and Technological Research Council of Turkey) Support Program for Scientific and Technological Research Projects grant number 221M243.

Data availability

Data will be made available on request.

References

[1] K.S. Suslick, D.A. Hammerton, R.E. Cline, Sonochemical hot spot, Journal of the American Chemical Society 108 (18) (1986) 5641–5642, https://doi.org/10.1021/ja00278a055.
[2] A.M. Abdelrahman, et al., The flow pattern effects of hydrodynamic cavitation on waste activated sludge digestibility, Chemosphere 357 (2024) 141949, https://doi.org/10.1016/J.CHEMOSPHERE.2024.141949.
[3] Y.M. Oo, A. Legwiriyakul, J. Thawornprasert, K. Somnuk, Production of diesel–biodiesel–water fuel nanoemulsions using three-dimensional printed rotor–stator hydrodynamic cavitation, Fuel 317 (2022), https://doi.org/10.1016/j.fuel.2022.123445.
[4] M. Jafarpour, A.S. Aghdam, M.T. Gevari, A. Koşar, M.K. Bayazit, M. Ghorbani, An ecologically friendly process for graphene exfoliation based on the 'hydrodynamic cavitation on a chip' concept, RSC Advances 11 (29) (2021) 17965–17975, https://doi.org/10.1039/d1ra03352b.
[5] L. Albanese, R. Ciriminna, F. Meneguzzo, M. Pagliaro, Beer-brewing powered by controlled hydrodynamic cavitation: Theory and real-scale experiments, Journal of Cleaner Production 142 (2017) 1457–1470, https://doi.org/10.1016/j.jclepro.2016.11.162.
[6] Y. Fang, D. Hariu, T. Yamamoto, S. Komarov, Acoustic cavitation assisted plasma for wastewater treatment: Degradation of Rhodamine B in aqueous solution, Ultrasonics Sonochemistry 52 (2019) 318–325, https://doi.org/10.1016/j.ultsonch.2018.12.003.
[7] N. Burshtein, S.T. Chan, K. Toda-Peters, A.Q. Shen, S.J. Haward, 3D-printed glass microfluidics for fluid dynamics and rheology, Current Opinion in Colloid and Interface Science 43 (2019) 1–14, https://doi.org/10.1016/J.COCIS.2018.12.005.
[8] H. Amini, W. Lee, D. Di Carlo, Inertial microfluidic physics, Royal Society of Chemistry (2014), https://doi.org/10.1039/c4lc00128a.
[9] K. Mao, et al., Paper-based microfluidics for rapid diagnostics and drug delivery, Journal of Controlled Release 322 (2020) 187–199, https://doi.org/10.1016/J.JCONREL.2020.03.010.
[10] R. Baviere, F. Ayela, S.Le Person, M. Favre-Marinet, Experimental characterization of water flow through smooth rectangular microchannels, Physics of Fluids 17 (9) (2005) 098105, https://doi.org/10.1063/1.2039667.
[11] V. Anand, J. David, I.C. Christov, Non-Newtonian fluid–structure interactions: Static response of a microchannel due to internal flow of a power-law fluid, Journal of Non-Newtonian Fluid Mechanics 264 (2019) 62–72, https://doi.org/10.1016/j.jnnfm.2018.12.008.
[12] L. Shui, J.C.T. Eijkel, A. van den Berg, Multiphase flow in micro- and nanochannels, Sensors & Actuators, B: Chemical 121 (1) (2007) 263–276, https://doi.org/10.1016/J.SNB.2006.09.040.

[13] A. Abidi, et al., A Review of the Methods of Modeling Multi-Phase Flows within Different Microchannels Shapes and Their Applications, Micromachines (Basel) 12 (9) (2021) 1113, https://doi.org/10.3390/mi12091113.

[14] L.E. O'Neill, I. Mudawar, Review of two-phase flow instabilities in macro- and micro-channel systems, International Journal of Heat and Mass Transfer 157 (2020) 119738, https://doi.org/10.1016/J.IJHEATMASSTRANSFER.2020.119738.

[15] C. Mishra, Y. Peles, An experimental investigation of hydrodynamic cavitation in micro-Venturis, Physics of Fluids 18 (10) (2006), https://doi.org/10.1063/1.2360996.

[16] P.R. Gogate, Cavitational reactors for process intensification of chemical processing applications: A critical review, Chemical Engineering and Processing: Process Intensification 47 (4) (2008) 515–527, https://doi.org/10.1016/J.CEP.2007.09.014.

[17] M. Omelyanyuk, A. Ukolov, I. Pakhlyan, N. Bukharin, M. El Hassan, Experimental and numerical study of cavitation number limitations for hydrodynamic cavitation inception prediction, Fluids 7 (6) (2022) 198, https://doi.org/10.3390/fluids7060198.

[18] E.V Ivanov, B.I. Gorbunov, A. Pasin, B. Arjutow, A.L. Novozhilov, Efficiency evaluation of cavitation heat generator used for desalination of saline solutions, Jurnal Kejuruteraan (2022) [Online]. Available, https://api.semanticscholar.org/CorpusID:254216643.

[19] X. Sun, et al., Experimental investigation of the thermal and disinfection performances of a novel hydrodynamic cavitation reactor, Ultrasonics Sonochemistry 49 (2018) 13–23, https://doi.org/10.1016/J.ULTSONCH.2018.02.039.

[20] M. Callenaere, J.-P. Franc, J.-M. Michel, M. Riondet, The cavitation instability induced by the development of a re-entrant jet, Journal of Fluid Mechanics 444 (2001) 223–256, https://doi.org/10.1017/S0022112001005420.

[21] T. Chen, H. Chen, W. Liang, B. Huang, L. Xiang, Experimental investigation of liquid nitrogen cavitating flows in converging-diverging nozzle with special emphasis on thermal transition, International Journal of Heat and Mass Transfer 132 (2019) 618–630, https://doi.org/10.1016/J.IJHEATMASSTRANSFER.2018.11.157.

[22] M. Petkovšek, M. Dular, IR measurements of the thermodynamic effects in cavitating flow, International Journal of Heat and Fluid Flow 44 (2013) 756–763, https://doi.org/10.1016/J.IJHEATFLUIDFLOW.2013.10.005.

[23] M. Dular, Hydrodynamic cavitation damage in water at elevated temperatures, Wear 346–347 (2016) 78–86, https://doi.org/10.1016/j.wear.2015.11.007.

[24] M. Petkovšek, M. Dular, Observing the thermodynamic effects in cavitating flow by IR thermography, Experimental Thermal and Fluid Science 88 (2017) 450–460, https://doi.org/10.1016/j.expthermflusci.2017.07.001.

[25] L. Chernin, R. Guobys, M. Vilnay, Factors affecting the procedure for testing cavitation erosion of GFRP composites using an ultrasonic transducer, Wear 530–531 (2023) 205059, https://doi.org/10.1016/J.WEAR.2023.205059.

[26] M. Ghorbani, G. Deprem, E. Ozdemir, A.R. Motezakker, L.G. Villanueva, A. Kosar, On 'Cavitation on Chip' in Microfluidic Devices with Surface and Sidewall Roughness Elements, Journal of Microelectromechanical Systems 28 (5) (2019) 890–899, https://doi.org/10.1109/JMEMS.2019.2925541.

[27] Q.ning SONG, et al., Selective phase corrosion and cavitation erosion behaviors of various copper alloys in 3.5 % NaCl solutions with different pH values, Transactions of Nonferrous Metals Society of China 33 (10) (2023) 3039–3053, https://doi.org/10.1016/S1003-6326(23)66316-2.

[28] A. Moshaii, R. Rezaei-Nasirabad, K. Imani, M. Silatani, R. Sadighi-Bonabi, Role of thermal conduction in single-bubble cavitation, Physics Letters A 372 (8) (2008) 1283–1287, https://doi.org/10.1016/J.PHYSLETA.2007.09.014.

[29] T. Chen, B. Huang, G. Wang, K. Wang, Effects of fluid thermophysical properties on cavitating flows, Journal of Mechanical Science and Technology 29 (10) (2015) 4239–4246, https://doi.org/10.1007/s12206-015-0920-5.

[30] J.-P. Franc, J.-M. Michel, Fundamentals of cavitation, 2005.

[31] C.E. Brennen, Cavitation and bubble dynamics, 2014.

[32] Y. Iga, J. Okajima, Y. Yamagichi, H. Sasaki, Y. Ito, Thermodynamic suppression effect of cavitation arising in a hydrofoil in 140 °C hot water, Journal of Fluids Engineering 145 (1) (2023), https://doi.org/10.1115/1.4055600.

[33] A. Cervone, C. Bramanti, E. Rapposelli, L. d'Agostino, Thermal Cavitation Experiments on a NACA 0015 Hydrofoil, Journal of Fluids Engineering 128 (2) (2005) 326–331, https://doi.org/10.1115/1.2169808.

[34] Z.Y. Zheng, et al., Experimental investigation of temperature effect on hydrodynamic characteristics of natural cavitation in rotational supercavitating evaporator for desalination, Renewable Energy 174 (2021) 278–292, https://doi.org/10.1016/J.RENENE.2021.04.038.

[35] D. Chakraborty, S. Chakraborty, Microfluidic Transport and Micro-scale Flow Physics: An Overview, in: S. Chakraborty (Ed.), Microfluidics and Microfabrication, Springer US, Boston, MA, 2010, pp. 1–85, https://doi.org/10.1007/978-1-4419-1543-6_1.

[36] M. Bossert, et al., Surface tension of cavitation bubbles, Proceedings of the National Academy of Sciences 120 (15) (2023), https://doi.org/10.1073/pnas.2300499120.

[37] C. Mishra, Y. Peles, Cavitation in flow through a micro-orifice inside a silicon microchannel, Physics of Fluids 17 (1) (2004) 013601, https://doi.org/10.1063/1.1827602.

[38] M. Ghorbani, A.K. Sadaghiani, L.G. Villanueva, A. Koşar, Hydrodynamic cavitation in microfluidic devices with roughened surfaces, Journal of Micromechanics and Microengineering 28 (7) (2018), https://doi.org/10.1088/1361-6439/aab9d0.

[39] F. Rokhsar Talabazar, A. Sheibani Aghdam, M. Jafarpour, D. Grishenkov, A. Koşar, M. Ghorbani, Chemical effects in 'hydrodynamic cavitation on a chip': The role of cavitating flow patterns, Chemical Engineering Journal 445 (2022), https://doi.org/10.1016/j.cej.2022.136734.

[40] M. Chen, L. Cheng, R. Cao, C. Lyu, A study to investigate fluid-solid interaction effects on fluid flow in micro scales, Energies (Basel) 11 (9) (2018), https://doi.org/10.3390/en11092197.

[41] F.Rokhsar Talabazar, et al., Design and fabrication of a vigorous 'cavitation-on-a-chip' device with a multiple microchannel configuration, Microsystems & Nanoengineering 7 (1) (2021) 44, https://doi.org/10.1038/s41378-021-00270-1.

[42] J.P. McHale, S.V. Garimella, Bubble nucleation characteristics in pool boiling of a wetting liquid on smooth and rough surfaces, International Journal of Multiphase Flow 36 (4) (2010) 249–260, https://doi.org/10.1016/j.ijmultiphaseflow.2009.12.004.

[43] H. Wu, H. Zheng, Y. Li, C.D. Ohl, H. Yu, D. Li, Effects of surface tension on the dynamics of a single micro bubble near a rigid wall in an ultrasonic field, Ultrasonics Sonochemistry 78 (2021) 105735, https://doi.org/10.1016/J.ULTSONCH.2021.105735.

[44] Z. Jávor, N. Schreithofer, K. Heiskanen, Multi-scale analysis of the effect of surfactants on bubble properties, Minerals Engineering 99 (2016) 170–178, https://doi.org/10.1016/J.MINENG.2016.09.026.

[45] L. Boubendir, S. Chikh, L. Tadrist, On the surface tension role in bubble growth and detachment in a micro-tube, International Journal of Multiphase Flow 124 (2020) 103196, https://doi.org/10.1016/J.IJMULTIPHASEFLOW.2019.103196.

[46] M. Ge, G. Zhang, M. Petkovšek, K. Long, O. Coutier-Delgosha, Intensity and regimes changing of hydrodynamic cavitation considering temperature effects, Journal of Cleaner Production 338 (2022), https://doi.org/10.1016/j.jclepro.2022.130470.

[47] S.J. Kline, Discussion: 'a practical application of uncertainty calculations to measured data' (Thrasher, L. W., and Binder, R. C., 1957, Trans. ASME, 79, pp. 373–375), Transactions of the American Society of Mechanical Engineers 79 (2) (2022) 375–376, https://doi.org/10.1115/1.4013018.

[48] T.J. O'Hern, An experimental investigation of turbulent shear flow cavitation, Journal of Fluid Mechanics 215 (1990) 365–391, https://doi.org/10.1017/S0022112090002683.

[49] E.S.C. Allan, L. Barbaca, J.A. Venning, P.S. Russell, B.W. Pearce, P.A. Brandner, Nucleation and cavitation inception in high Reynolds number shear layers, Physics of Fluids 35 (1) (2023), https://doi.org/10.1063/5.0132054.

[50] I. Castellani, Cavity length and re-entrant jet in 2-D sheet cavitation, 52, 2006, https://doi.org/10.2495/AFM06034.

[51] Y. Zhao, G. Wang, B. Huang, Vortex structure analysis of unsteady cloud cavitating flows around a hydrofoil, Modern Physics Letters B 30 (02) (2016) 1550275, https://doi.org/10.1142/S0217984915502759.

[52] M. Ge, P. Manikkam, J. Ghossein, R. Kumar Subramanian, O. Coutier-Delgosha, G. Zhang, Dynamic mode decomposition to classify cavitating flow regimes induced by thermodynamic effects, Energy 254 (2022) 124426, https://doi.org/10.1016/j.energy.2022.124426.

[53] O. Coutier-Delgosha, J.-F. Devillers, T. Pichon, A. Vabre, R. Woo, S. Legoupil, Internal structure and dynamics of sheet cavitation, Physics of Fluids 18 (1) (2006) 017103, https://doi.org/10.1063/1.2149882.

[54] K. Agarwal, O. Ram, J. Katz, Cavitating Structures at Inception in Turbulent Shear Flow, in: Proceedings of the 10th International Symposium on Cavitation (CAV2018), ASME Press, 2018, p. 0, https://doi.org/10.1115/1.861851_ch33. J. Katz, Ed.

[55] S. Yamada, General shear-thinning dynamics of confined fluids, Tribology Letters (2002).

[56] B. Stutz, J.L. Reboud, Two-phase flow structure of sheet cavitation, Physics of Fluids 9 (12) (1997) 3678–3686, https://doi.org/10.1063/1.869505.

[57] M. van Rijsbergen, A review of sheet cavitation inception mechanisms, in: 16th International Symposium on Transport Phenomena and Dynamics of Rotating Machinery, Honolulu, United States, 2016 [Online]. Available, https://hal.science/hal-01890067.

[58] M.Y. Ha, C.H. Kim, Y.W. Jung, S.G. Heo, Two-phase flow analysis in multi-channel, Journal of Mechanical Science and Technology 20 (6) (2006) 840–848, https://doi.org/10.1007/BF02915947.

[59] S. Dutta, T.E. Tokyay, Y.A. Cataño-Lopera, S. Serafino, M.H. Garcia, Application of computational fluid dynamic modelling to improve flow and grit transport in Terrence J. O'Brien Water Reclamation Plant, Chicago, Illinois, Journal of Hydraulic Research 52 (6) (2014) 759–774, https://doi.org/10.1080/00221686.2014.949883.

[60] P.F. Pelz, T. Keil, T.F. Gro, The transition from sheet to cloud cavitation, Journal of Fluid Mechanics 817 (2017) 439–454, https://doi.org/10.1017/jfm.2017.75.

[61] U. Gawandalkar, C. Poelma, The structure of near-wall re-entrant flow and its influence on cloud cavitation instability, Experiments in Fluids 63 (5) (2022) 77, https://doi.org/10.1007/s00348-022-03417-6.

[62] J.P. Franc, E. Janson, P. Morel, C. Rebattet, M. Riondet, Visualizations of leading edge cavitation in an inducer at different temperatures, 2001.

[63] M.G. De Giorgi, A. Ficarella, Simulation of cryogenic cavitation by using both inertial and heat transfer control bubble growth, in: *39th AIAA Fluid Dynamics Conference*, in Fluid Dynamics and Co-located Conferences, American Institute of Aeronautics and Astronautics, 2009, https://doi.org/10.2514/6.2009-4039.

[64] E. Khoshbakhtnejad, F.B. Golezani, B. Mohammadian, A.H.A. Yassine, H. Sojoudi, Trajectory and impact dynamics of snowflakes: Fundamentals and applications, Powder Technology 448 (2024) 120298, https://doi.org/10.1016/J.POWTEC.2024.120298.

[65] J.-P. Franc, C. Rebattet, A. Coulon, An experimental investigation of thermal effects in a cavitating inducer, Journal of Fluids Engineering 126 (5) (2004) 716–723, https://doi.org/10.1115/1.1792278.

[66] J. Kim, S.J. Song, Measurement of thermal parameter and Reynolds number effects on cavitation instability onset in a turbopump inducer, Journal of the Global Power and Propulsion Society 1 (2017), https://doi.org/10.22261/H5DYU3 p. H5DYU3.
[67] Y. Li, Study on the properties of water molecule at different temperatures, Journal of Physics. Conference Series 2206 (1) (2022) 012031, https://doi.org/10.1088/1742-6596/2206/1/012031.
[68] H. Fang, K. Ni, J. Wu, J. Li, L. Huang, D. Reible, The effects of hydrogen bonding on the shear viscosity of liquid water, International Journal of Sediment Research 34 (1) (2019) 8–13, https://doi.org/10.1016/j.ijsrc.2018.10.008.
[69] M. Omelyanyuk, A. Ukolov, I. Pakhlyan, N. Bukharin, M. El Hassan, Experimental and numerical study of cavitation number limitations for hydrodynamic cavitation inception prediction, Fluids 7 (6) (2022) 198, https://doi.org/10.3390/fluids7060198.
[70] M. Ge, C. Sun, G. Zhang, O. Coutier-Delgosha, D. Fan, Combined suppression effects on hydrodynamic cavitation performance in Venturi-type reactor for process intensification, Ultrasonics Sonochemistry 86 (2022), https://doi.org/10.1016/j.ultsonch.2022.106035.
[71] C. Mishra, Y. Peles, Cavitation in flow through a micro-orifice inside a silicon microchannel, Physics of Fluids 17 (1) (2004) 013601, https://doi.org/10.1063/1.1827602.
[72] X. He, X. Song, J. Zhang, H. Peng, S. Zhou, Deciphering surface tension effects of double cavitation bubbles interaction: A lattice Boltzmann study, International Journal of Thermal Sciences 189 (2023) 108266, https://doi.org/10.1016/J.IJTHERMALSCI.2023.108266.
[73] M. Ge, M. Petkovšek, G. Zhang, D. Jacobs, O. Coutier-Delgosha, Cavitation dynamics and thermodynamic effects at elevated temperatures in a small Venturi channel, International Journal of Heat and Mass Transfer 170 (2021) 120970, https://doi.org/10.1016/j.ijheatmasstransfer.2021.120970.
[74] C. Kleinstreuer, J. Li, J. Koo, Microfluidics of nano-drug delivery, International Journal of Heat and Mass Transfer 51 (23–24) (2008) 5590–5597, https://doi.org/10.1016/j.ijheatmasstransfer.2008.04.043.
[75] N.A. Bulychev, Application of intensive hydrodynamic cavitation in liquids for synthesis of hydrogen and nanoparticles, International Journal of Hydrogen Energy 46 (41) (2021) 21298–21302, https://doi.org/10.1016/j.ijhydene.2021.04.019.